



ISTITUTO NAZIONALE DI RICERCA METROLOGICA Repository Istituzionale

Fast high-resolution electric properties tomography using three-dimensional quantitative transient-state imaging-based water fraction estimation

Original

Fast high-resolution electric properties tomography using three-dimensional quantitative transient-state imaging-based water fraction estimation / Cencini, Matteo; Lancione, Marta; Pasquariello, Rosa; Peretti, Luca; Pirkel, Carolin M.; Schulte, Rolf F.; Buonincontri, Guido; Arduino, Alessandro; Zilberti, Luca; Biagi, Laura; Tosetti, Michela. - In: NMR IN BIOMEDICINE. - ISSN 0952-3480. - 37:1(2023), p. e5039. [10.1002/nbm.5039]

Availability:

This version is available at: 11696/78819 since: 2024-02-14T09:10:54Z

Publisher:

WILEY

Published

DOI:10.1002/nbm.5039

Terms of use:


This article is made available under terms and conditions as specified in the corresponding bibliographic description in the repository

Publisher copyright

(Article begins on next page)

RESEARCH ARTICLE

Fast high-resolution electric properties tomography using three-dimensional quantitative transient-state imaging-based water fraction estimation

Matteo Cencini¹ | Marta Lancione²  | Rosa Pasquariello² | Luca Peretti² |
 Carolin M. Pirkel³ | Rolf F. Schulte³ | Guido Buonincontri² | Alessandro Arduino⁴ |
 Luca Zilberti⁴ | Laura Biagi² | Michela Tosetti²

¹Istituto Nazionale di Fisica Nucleare, Sezione di Pisa, Pisa, Italy

²IRCCS Stella Maris, Pisa, Italy

³GE HealthCare, Munich, Germany

⁴Istituto Nazionale di Ricerca Metrologica (INRiM), Torino, Italy

Correspondence

Laura Biagi, IRCCS Stella Maris, Pisa, Italy.
 Email: laura.biagi@fsm.unipi.it

Funding information

European Metrology Programme for Innovation and Research (EMPIR); European Union's Horizon 2020 Research and Innovation Programme, Grant/Award Number: 18HLT05QUIERO; Italian Ministry of Health, Grant/Award Number: RCLinea4

Abstract

In this study, we aimed to develop a fast and robust high-resolution technique for clinically feasible electrical properties tomography based on water content maps (wEPT) using Quantitative Transient-state Imaging (QTI), a multiparametric transient state-based method that is similar to MR fingerprinting. Compared with the original wEPT implementation based on standard spin-echo acquisition, QTI provides robust electrical properties quantification towards B_1^+ inhomogeneities and full quantitative relaxometry data. To validate the proposed approach, 3D QTI data of 12 healthy volunteers were acquired on a 1.5 T scanner. QTI-provided T_1 maps were used to compute water content maps of the tissues using an empirical relationship based on literature ex-vivo measurements. Assuming that electrical properties are modulated mainly by tissue water content, the water content maps were used to derive electrical conductivity and relative permittivity maps. The proposed technique was compared with a conventional phase-only Helmholtz EPT (HH-EPT) acquisition both within whole white matter, gray matter, and cerebrospinal fluid masks, and within different white and gray matter subregions. In addition, QTI-based wEPT was retrospectively applied to four multiple sclerosis adolescent and adult patients, compared with conventional contrast-weighted imaging in terms of lesion delineation, and quantitatively assessed by measuring the variation of electrical properties in lesions. Results obtained with the proposed approach agreed well with theoretical predictions and previous in vivo findings in both white and gray matter. The reconstructed maps showed greater anatomical detail and lower variability compared with standard phase-only HH-EPT. The technique can potentially improve delineation of pathology when compared with conventional contrast-weighted imaging and was able to detect significant variations in lesions with respect to normal-appearing tissues. In

Abbreviations: ANTs, advanced normalization tools; bSSFP, balanced steady-state free precession; CSF, cerebrospinal fluid; EPT, electrical properties tomography; FLAIR, Fluid Attenuated Inversion Recovery; FSL, FMRIB Software Library; FSPGR, Fast Spoiled Gradient-echo; GM, gray matter; HH-EPT, Helmholtz EPT; MRF, MR fingerprinting; MR-STAT, MR-Spin Tomography in Time domain; QTI, Quantitative Transient-state Imaging; R, radiofrequency; TE, echo time; TR, repetition time; wEPT, water content-based EPT; WM, white matter.

This is an open access article under the terms of the [Creative Commons Attribution-NonCommercial](https://creativecommons.org/licenses/by-nc/4.0/) License, which permits use, distribution and reproduction in any medium, provided the original work is properly cited and is not used for commercial purposes.

© 2023 The Authors. *NMR in Biomedicine* published by John Wiley & Sons Ltd.

conclusion, QTI can reliably measure conductivity and relative permittivity of brain tissues within a short scan time, opening the way to the study of electric properties in clinical settings.

KEYWORDS

electric properties tomography, electrical conductivity, MR fingerprinting, quantitative MR imaging, relative permittivity, transient-state imaging

1 | INTRODUCTION

Quantitative MRI allows for noninvasive high-resolution tissue characterization, potentially improving the accuracy and reproducibility of the diagnosis and enabling longitudinal assessment of the disease progression and treatment in both children and adults. To date, many MR-based techniques for the quantification of several tissue physical properties have been demonstrated, including T_1 and T_2 relaxometry, diffusion, perfusion, and magnetic susceptibility. Other important parameters for tissue characterization are its electrical properties, i.e., electrical conductivity and relative permittivity. Strong variations of electrical conductivity have been reported in cancerous tissues^{1,2} and in the presence of vascular diseases (e.g., myocardial infarction³ and stroke⁴). In addition, electrical properties can be used to predict subject-specific local specific absorption rate (SAR) maps for the assessment of safety in radiofrequency (RF) pulse design.⁵ MR-based electric properties tomography (MR-EPT) is a relatively recent technique that was developed to noninvasively map the distribution of electrical conductivity and relative permittivity in the tissues.⁶

Common approaches to MR-EPT rely on the effect of the electrical properties on the transmit RF field (B_1^+) spatial distribution.^{7,8} Because the electrical properties of biological tissues are dispersive in frequency, that is, they depend on the frequency of the electromagnetic field to which the sample is exposed, MR-based methods measure the electrical properties within the range of megahertz (i.e., the frequency of the RF field used by the MR scanner). The MR-EPT processing typically involves second-order derivatives of the complex B_1^+ map,⁹ resulting in noise amplification and region boundary errors, hampering quantification in regions with convoluted edges, for example, gray matter (GM) and cerebrospinal fluid (CSF) in brain MRI.

A possible solution to these issues has been proposed by Michel et al.,¹⁰ with the so-called water content-based Electric Properties Tomography (wEPT) approach. This approach relies on the fact that, at high frequencies, cell membranes exhibit low impedance, allowing propagation of RF electric currents associated with the B_1^+ field. Therefore, in this regime, tissue electrical properties are modulated by their water and ionic content. Assuming that, in living tissues, the latter is kept constant by homeostasis, electrical properties can be determined by measuring the tissue water content, which in turn is highly correlated with the tissue longitudinal relaxation time, T_1 .¹¹ Several studies have successfully applied this approach at different frequency ranges,^{12,13} and tested its validity in vivo.¹⁴ In these implementations, the ratio between two T_1 -weighted spin-echo (SE) images was used to compute an approximate T_1 map and then used to estimate tissue electrical properties. This enables easy deployment in a clinical setting, but may introduce a spatially varying bias due to B_1^+ field inhomogeneities.¹⁵ This limitation can be circumvented by using more robust approaches to estimate the T_1 of the tissues and consequently the corresponding water content. Examples of these approaches are magnetic resonance (MR) fingerprinting,¹⁶ MR-Spin Tomography in Time domain (MR-STAT),¹⁷ and Quantitative Transient-state Imaging¹⁸ (QTI), which rely on the transient state of the MR response to achieve robust T_1 and T_2 quantification, while maintaining a short scan time, i.e., comparable with that for a conventional contrast-weighted image. These techniques demonstrated excellent repeatability and reproducibility at different field strengths both in vitro and in vivo,^{19–23} and provide robust T_1 quantification towards B_0 and B_1^+ field inhomogeneities.²⁴

In this work, we aimed to demonstrate that QTI-derived T_1 maps can be used to achieve reliable electrical properties estimations in vivo at clinical field strength (1.5 T). To this purpose, we acquired QTI data of 12 healthy volunteers and compared the resulting electrical properties map with the expected theoretical values in white matter (WM), GM, and CSF. In addition, we retrieved standard transmit field-based EPT maps and compared the two approaches in terms of consistency with respect to literature-based reference values and spatial variability. Finally, we applied the QTI-based wEPT method to a small group of multiple sclerosis (MS) patients, to evaluate its capability in detecting variations of the electrical properties in the lesions compared with the surrounding normal-appearing tissue.

2 | METHODS

2.1 | QTI acquisition and reconstruction

Twelve healthy subjects (five males, seven females, age 29–55 years) were scanned on a GE HealthCare HDxt 1.5 T system using a quadrature-mode body coil for transmission and an eight-channel head coil for reception, in compliance with local ethical approval. Each

subject underwent a 3D steady-state free precession QTI acquisition, as described in previous work.^{25,26} The QTI implementation consisted of an inversion-prepared variable flip angle, with fixed TE (0.5 ms) and TR (8.5 ms), corresponding to a total scan time of 7 min. k-space sampling was performed using a 3D spiral projection trajectory (field of view = $225 \times 225 \times 225$ mm³; voxel size = $1.125 \times 1.125 \times 1.125$ mm³), with unbalanced gradients along z to reduce B₀ sensitivity.²⁷ Images were reconstructed offline using a zero-filled low-rank subspace reconstruction,²⁸ followed by a fully connected neural network T₁, T₂, and M₀ estimation.²⁵

2.2 | Water-based EPT reconstruction

Electrical conductivity σ and relative permittivity ϵ_r were obtained from QTI-derived T₁ maps as follows (Figure 1): first, water content W in the range 0–1 was obtained according to Fatouros and Marmarou¹¹

$$\frac{1}{W} = A + \frac{B}{T_1}, \quad (1)$$

where A and B are the fit constants that depend on the magnetic field strength and are equal to 0.935 and 341 ms at 1.5 T, respectively.¹¹

The QTI-based wEPT electrical properties σ^{wEPT} and ϵ_r^{wEPT} were then derived from the water content W via¹⁰

$$\sigma^{\text{wEPT}} = c_1 + c_2 \cdot \exp(c_3 \cdot W) \quad (2a)$$

$$\epsilon_r^{\text{wEPT}} = p_1 \cdot W^2 + p_2 \cdot W + p_3. \quad (2b)$$

Since the available literature values¹⁰ for the model coefficients were obtained at 3 T, here we repeated the calibration for a 1.5 T field strength. Specifically, calibration was performed by fitting the average literature water content²⁹ for WM, GM, and CSF against their theoretical conductivity and relative permittivity values at 64 MHz (i.e., Larmor frequency at 1.5 T) calculated with a fourth order Cole–Cole model³⁰:

$$\epsilon_r^C(\omega) = \epsilon_\infty + \sum_{n=1}^4 \frac{\Delta\epsilon_n}{1 + (i\omega\tau_n)^{1-a_n}} + \frac{\sigma_i}{i\omega\epsilon_0}, \quad (3)$$

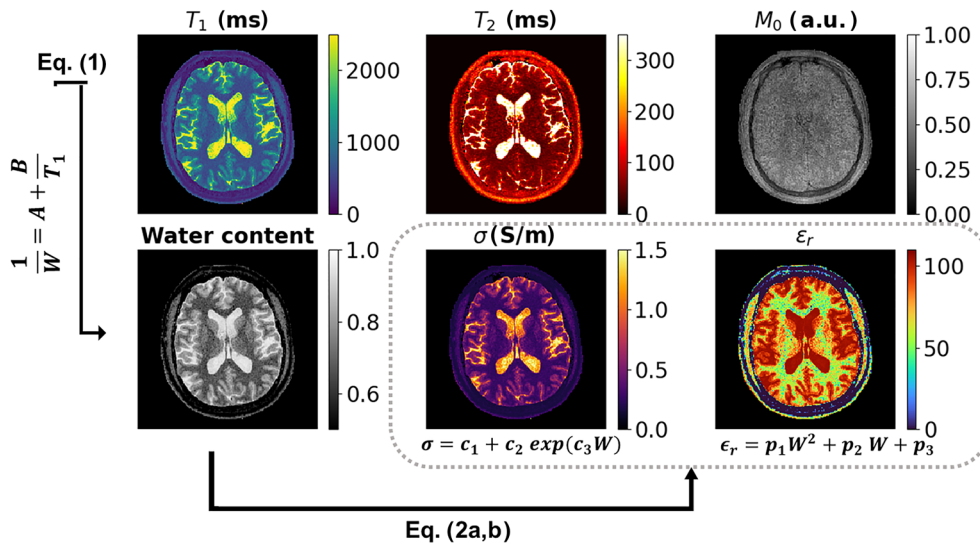


FIGURE 1 Processing pipeline to obtain electrical properties maps from a QTI-derived T₁ map. The first row shows the T₁, T₂, and M₀ maps obtained by QTI acquisition and reconstruction. The T₁ map is converted into a water content (W) map. Then the water content map is used to retrieve the electrical properties σ and ϵ_r . Calibration coefficients between electric properties and water curve are obtained by fitting literature-based water content values for WM, GM, and CSF against their theoretical predictions calculated with a fourth order Cole–Cole model. CSF, cerebrospinal fluid; GM, gray matter; QTI, Quantitative Transient-state Imaging; WM, white matter.

where $\epsilon_r^C(\omega) = \epsilon_r(\omega) - \frac{\sigma(\omega)}{i\omega\epsilon_0}$ is the complex relative permittivity. The Cole–Cole model coefficients (ϵ_∞ , $\Delta\epsilon_n$, τ_n , α_n , and σ_i) are reported (Table S1), as well as the corresponding electrical properties and water content values for the three calibration tissues (Table S2).

The resulting calibration coefficients c_1 , c_2 , c_3 and p_1 , p_2 , p_3 were 0.14, 0.0005 S/m, 8.3 and -870 , 1565 , -598 , respectively, and the corresponding fitting models are reported in Figure S1 together with the variation of electrical properties of WM, GM, and CSF as a function of the field strength according to the fourth-order Cole–Cole model.

2.3 | Conventional EPT acquisition and reconstruction

To validate the proposed approach, the acquisition protocol also included a whole-brain 3D balanced steady-state free precession (bSSFP) complex-valued image (voxel size = $2 \times 2 \times 2$ mm³, TE/TR = 1.5 ms/5.3 ms, flip angle = 30°, four averages, scan duration: 3 min 14 s) acquired using the scanner quadrature body coil for both transmission and reception and an inversion-prepared 3D Fast Spoiled GRAdient-echo (FSPGR) T₁-weighted acquisition (whole-brain coverage, voxel size = $1 \times 1 \times 1$ mm³, TE/TR = 5.16 ms/12.4 ms, TI = 700 ms, flip angle = 10°, scan duration: 7 min 18 s), obtained with the eight-channel head coil for signal reception.

These acquisitions were used to obtain conventional MR-based conductivity maps as follows³¹ (Figure 2). First, the bSSFP image was preprocessed by applying Gibbs ringing removal and 3D phase unwrapping, and FSPGR was segmented using a statistical parametric map,³² obtaining tissue probability maps for WM, GM, and CSF. These tissue maps were aligned to the bSSFP coordinate space with an affine transformation estimated using FSPGR and bSSFP magnitude images, and the FMRIB Software Library (FSL).³³ They were then converted to binary masks by assigning each voxel to the tissue class with the highest probability. Conductivity values were estimated from bSSFP phase ψ within the WM/GM/CSF masks independently, by solving the following equation:

$$\sigma^{HH-EPT} = \frac{\nabla^2 \psi}{2\omega\mu_0}, \quad (4)$$

where $\omega = 2\pi \cdot 64 \cdot 10^6 \frac{\text{rad}}{\text{s}}$ is the Larmor angular frequency at 1.5 T and μ_0 is the vacuum magnetic permeability. This approach is called phase-only Helmholtz EPT^{9,34} (HH-EPT). The Laplacian operator in Equation (4) was evaluated by fitting a local parabola within a spherical kernel of 14-voxels diameter centered on each target voxel.³¹ To reduce contamination from residual voxels belonging to different tissue classes, each voxel within the kernel was weighted according to the absolute difference in bSSFP magnitude compared with the target voxel using a Gaussian function,³⁵ whose standard deviation was empirically set to 0.25 (image magnitude units) for WM/CSF and 0.75 (image magnitude units) for GM. Finally, a local median filter was applied within the same kernel used for Laplacian evaluation and the estimated conductivities for WM/GM/CSF were merged in a single conductivity map.

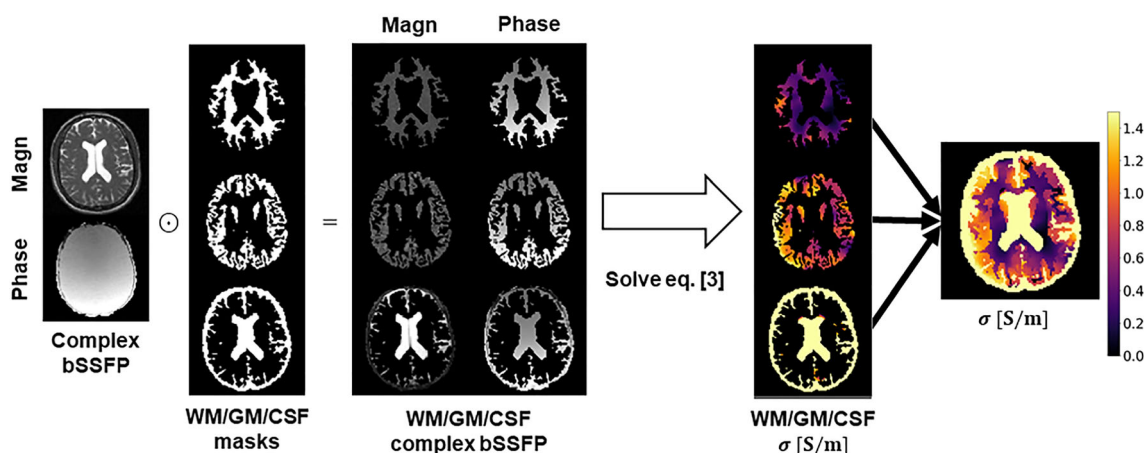


FIGURE 2 Processing steps required to obtain the bSSFP-based HH-EPT conductivity maps used as a reference: the bSSFP phase is multiplied by WM/GM/CSF binary masks obtained by segmentation of a separate T₁-weighted scan, the conductivity is computed independently for the three tissues, and the results are merged in a single conductivity map. bSSFP, balanced steady-state free precession; CSF, cerebrospinal fluid; GM, gray matter; HH-EPT, Helmholtz electrical properties tomography; WM, white matter.

2.4 | Analysis

Both QTI-based wEPT and bSSFP-based HH-EPT maps for each subject were nonrigidly aligned to a common coordinate space defined by the Montreal Neurological Institute (MNI) template via a two-step registration. First, EPT maps for each subject were coregistered to the corresponding FSPGR T_1 -weighted image using the QTI-based T_1 map and bSSFP magnitude, respectively, to estimate the alignment via FSL.³³ Then the FSPGRs were nonlinearly aligned to the MNI coordinate space using advanced normalization tools (ANTs)³⁶ software, and the resulting transformations were applied to the EPT maps and to the WM/GM/CSF probabilistic maps. WM, GM, and CSF binary masks were obtained by selecting a probability threshold of 70%, and median values within each tissue for each subject were computed for both QTI- and bSSFP-based EPT maps. In addition, median conductivity values were computed for each subject within regions of interest (ROIs) from the USCLobes Atlas^{37,38} that were masked using WM and GM masks and from a Freesurfer segmentation of the MNI template. In particular, six subcortical WM ROIs (frontal, parietal, temporal and occipital WM, cingulate tract and cerebellum WM), and seven cortical GM ROIs (frontal, parietal, temporal and occipital GM, cingulate gyrus, cerebellum GM and insular cortex) were obtained from the USCLobes Atlas, whereas the ROIs for nine deep WM/GM structures (splenium and genu of corpus callosum, midbrain, pons, medulla, caudate nucleus, globus pallidus, putamen, and thalamus) were derived from the Freesurfer segmentation (Figure 3). The caudate nucleus, globus pallidus, putamen, thalamus and all subcortical WM and cortical GM ROIs except for cerebellum were divided into left and right hemispheres. wEPT and HH-EPT data were compared using Pearson's correlation and Bland-Altman analysis. In addition, both were compared with the fourth-order Cole-Cole predictions of WM and GM conductivities and with previous in vivo phase-only HH-EPT findings at 1.5 T. Specifically, we used the pooled standard deviation of the conductivity values measured by Voigt et al.³⁴ as an estimate of the expected WM and GM variability. A similar subregion analysis was performed for the relative permittivity values obtained with the QTI-based wEPT method. Because phase-only HH-EPT does not provide an independent measurement of relative permittivity, QTI-based wEPT results were compared with theoretical WM and GM predictions and evaluated in terms of intersubject variability by calculating the interquartile range for each ROI.

Both electrical conductivity and relative permittivity measurements obtained via QTI-based wEPT were also compared with the original SE-based wEPT implementation from Michel et al.¹⁰ To enable the comparison, we used the water content values reported in Michel et al. to estimate conductivity and relative permittivity values at 1.5 T field strength. We grouped the left and right hemispheres and restricted the comparison to the deep WM/GM ROIs, i.e., those which were included in the Michel et al. publication, and we calculated the Pearson's correlation between QTI-based and SE-based wEPT measurements.

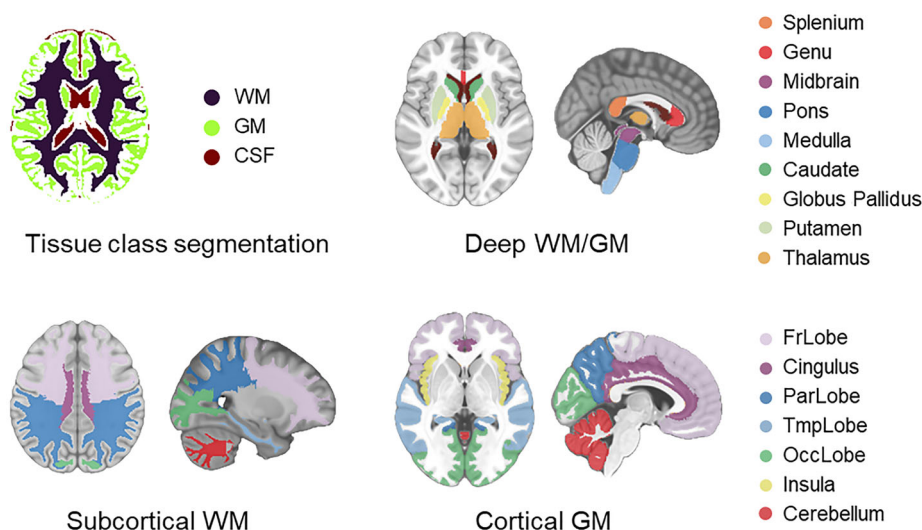


FIGURE 3 ROIs chosen for the wEPT validation: wEPT and HH-EPT conductivity values were measured in the whole WM/GM/CSF masks and in several subregions of subcortical WM, cortical GM, and deep WM/GM. Subcortical WM and cortical GM regions were obtained by multiplying the corresponding USCLobes Atlas ROIs by the WM and GM masks, whereas deep WM/GM ROIs were derived by segmenting the T_1 -weighted MNI image using Freesurfer. CSF, cerebrospinal fluid; GM, gray matter; HH-EPT, Helmholtz electrical properties tomography; MNI, Montreal Neurological Institute; ROI, region of interest; wEPT, water content-based electrical properties tomography; WM, white matter.

2.5 | Application to multiple sclerosis

Three-dimensional QTI data of four adolescent and adult MS patients (two males, two females, aged 15–60 years) were retrospectively processed to obtain wEPT conductivity and relative permittivity maps. Acquisition, reconstruction, and processing pipeline were the same as in the healthy volunteers' experiment. The maps were qualitatively assessed in terms of lesion identification capability when compared with conventional FLAIR Attenuated Inversion Recovery (FLAIR) contrast-weighted images. Here, FLAIR images had a similar resolution to the QTI acquisition. Specifically, FLAIR imaging parameters were voxel size = $1 \times 1 \times 1 \text{ mm}^3$, matrix size = 256×256 , number of slices = 184, TE/TR = 120.5 ms/6000 ms, inversion time = 1874 ms, and ASSET acceleration factor = 2. In addition, spherical ROIs were manually positioned in the FLAIR images in correspondence of MS lesions and coregistered to the QTI space using FSL. Then the average electrical properties values within these ROIs were quantitatively compared with the measurements within ROIs placed in the normal-appearing WM of the patients using a Mann–Whitney *U* test. Overall, two lesions and two control spherical ROIs of six-voxels diameter were selected for each subject.

3 | RESULTS

As shown in Figure 4, we successfully obtained conductivity maps of the tissues both using standard bSSFP-based phase-only HH-EPT and QTI-based wEPT, which also provided relative permittivity maps. While the inclusion of prior anatomical information mitigated the tissue border effect and the use of large derivative kernels significantly reduced noise amplification in the HH-EPT conductivity estimation, wEPT measurement provided a more uniform conductivity map and a higher level of anatomical detail. In addition, wEPT provided an estimate of the relative permittivity of the tissue, which cannot be obtained using phase-only HH-EPT.

Quantitative data are reported in Table 1. HH-EPT tended to overestimate conductivity values in WM and GM with respect to reference predictions based on the fourth-order Cole–Cole model: averaged across the subject cohort, median HH-EPT conductivity values in WM/GM/CSF were 0.47 ± 0.04 , 0.77 ± 0.07 , and $1.9 \pm 0.5 \text{ S/m}$, respectively, while the corresponding reference values are 0.29, 0.51, and 2.06 S/m. Nevertheless, these estimations were within the range of previous in vivo reports.³⁴ On the other hand, wEPT-based estimations agreed with reference values within 10%, except for conductivity in the CSF region, which was underestimated by approximately 60%. Figure 5 reports the results of the subregion analysis. Measurements for the two techniques showed similar inter-region heterogeneity trends in all ROIs, with values clustered around WM/GM predictions for subcortical WM and cortical GM, respectively, and ranging from WM to GM for deep WM and GM structures. Again, HH-EPT-based conductivity values were overestimated with respect to the reference but consistent with previous in vivo reports. Conductivity measurements showed similar variability within all subcortical WM ROIs, with an average interquartile range of 0.09 S/m excluding the cerebellum (interquartile range = 0.33 S/m), while cortical GM and deep WM/GM ROIs exhibited increased variability with an average interquartile range of 0.16 and 0.26 S/m, respectively. Conversely, wEPT-based conductivity estimates were close to the expected values within 10% and were characterized by a lower variability in all ROIs, resulting in a narrow distribution across subjects with an average interquartile range lower than 0.025 S/m.

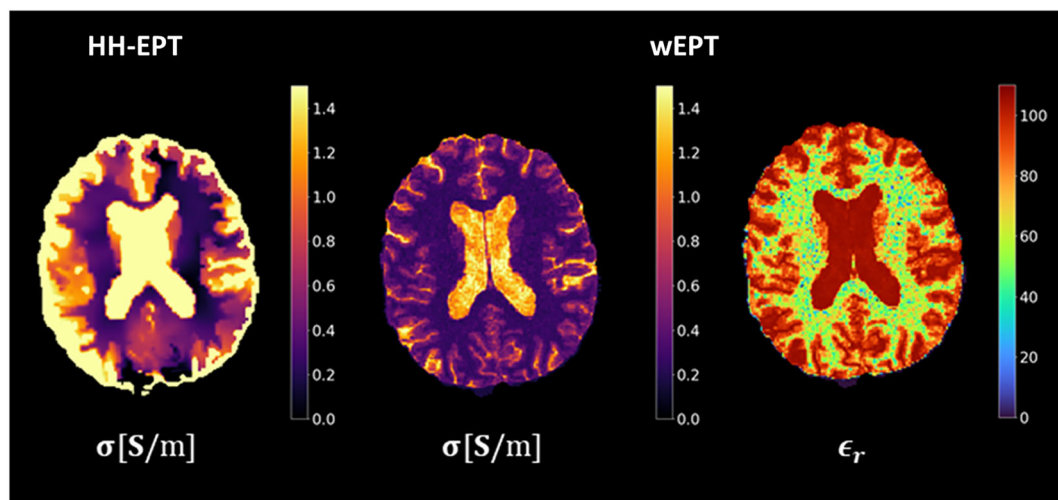


FIGURE 4 Representative conductivity map obtained with conventional phase-only HH-EPT and the corresponding conductivity (σ) and permittivity maps (ϵ_r) obtained using QTI-based wEPT. HH-EPT, Helmholtz electrical properties tomography; QTI, Quantitative Transient-state Imaging; wEPT, water content-based electrical properties tomography.

TABLE 1 Average across subject population of median EPT values within WM/GM/CSF masks obtained with bSSFP-based HH-EPT (conductivity only) and QTI-based wEPT (conductivity and relative permittivity), in comparison with their theoretical predictions based on a fourth order Cole–Cole model. Uncertainties were calculated as the standard deviation across subjects of the median WM/GM/CSF electrical properties values.

Conductivity (S/m)	WM	GM	CSF
Theoretical	0.29	0.51	2.06
wEPT	0.27 ± 0.01	0.46 ± 0.01	0.8 ± 0.1
HH-EPT	0.47 ± 0.04	0.77 ± 0.07	1.9 ± 0.5
Relative permittivity	WM	GM	CSF
Theoretical	68	97	97
wEPT	61 ± 3	93 ± 1	103 ± 1

Abbreviations: bSSFP, balanced steady-state free precession; CSF, cerebrospinal fluid; EPT, electrical properties tomography; GM, gray matter; HH-EPT, Helmholtz EPT; QTI, Quantitative Transient-state Imaging; wEPT, water content-based EPT; WM, white matter.

The median conductivity values of each box for HH-EPT and wEPT were compared in the Bland–Altman and correlation analysis shown in Figure 6. HH-EPT estimates were consistently higher than those for wEPT, leading to an average bias of 0.25 S/m, and values in both cortical GM and deep WM/GM regions were affected by a wider spread compared with subcortical WM, consistent with the results of the box plot analysis. Despite the high variability of HH-EPT conductivity measurements among similar brain regions, we found a moderate Pearson's correlation of 0.67 between the two techniques.

Results of subregion analysis for wEPT-based relative permittivity measurements are reported in Figure 7. As for the conductivity, wEPT relative permittivity showed good consistency with the theoretical values and low variability between subjects: the average difference with respect to theoretical predictions was lower than 10% in subcortical WM and cortical GM ROIs, and the interquartile range was lower than 4 in all of the considered ROIs.

Electrical properties at 64 MHz calculated from the water content values reported by Michel et al.¹⁰ are compared with QTI-based wEPT results in Figure 8. QTI-based wEPT provided consistently lower conductivity and relative permittivity values compared with the original SE implementation. Despite this difference, the two implementations exhibited a strong Pearson's correlation for both conductivity (0.94) and relative permittivity (0.87).

Finally, an application of QTI-based wEPT to the assessment of lesions in MS patients is shown in Figure 9. A representative example of lesion is shown in Figure 9A: it can be seen that the MS lesion has higher conductivity and relative permittivity values compared with the surrounding WM in the wEPT acquisition. Qualitatively, the lesions identified using FLAIR were also found in QTI-based wEPT maps. Quantitatively, as reported in Figure 9B, median conductivity and relative permittivity across all MS lesions were significantly higher than normal-appearing tissues ($p < 0.001$). Specifically, the median conductivity and relative permittivity values were 0.27 S/m and 59 in normal-appearing WM, respectively, similar to the results obtained for healthy volunteers. Instead, median electrical conductivity and relative permittivity were 0.45 S/m and 85 within the lesions, corresponding to a 66% and 44% increase, respectively.

4 | DISCUSSION

In this work, we demonstrated that QTI T_1 maps can be used to estimate high quality conductivity and relative permittivity maps of the human brain at 1.5 T. To the best of our knowledge, this is the first application of a transient-state method to the estimation of electrical properties. The reconstructed maps showed high consistency compared with the corresponding reference values: both conductivity and relative permittivity agreed to within 10% with the expected values, except for the estimated conductivity in CSF, which was underestimated by approximately 60%. This limitation of QTI-based wEPT can be attributed to an intrinsic T_1 underestimation for long T_1 values, which has also been observed in other studies using similar transient state-based acquisitions.²³ Importantly, our wEPT implementation appeared promising in capturing the heterogeneity within the different regions belonging to the same tissue class. Such heterogeneity has been reported in other studies analyzing brain myelination,³⁹ iron⁴⁰ and water²⁹ content, and sodium concentration.⁴¹ Since water content and sodium concentration are the main factors that determine electrical properties, we anticipate that variation in the former would be reflected in the latter. For example, for deep GM ROIs such as the caudate nucleus, putamen, and thalamus, which consist of GM structures with embedded myelinated axons, we found intermediate conductivity and relative permittivity between WM and GM theoretical predictions. This is consistent with previous reports for water content²⁹ and sodium concentration.⁴¹ Conventional phase-only HH-EPT acquisition also provided conductivity maps of the tissues. Measured conductivity

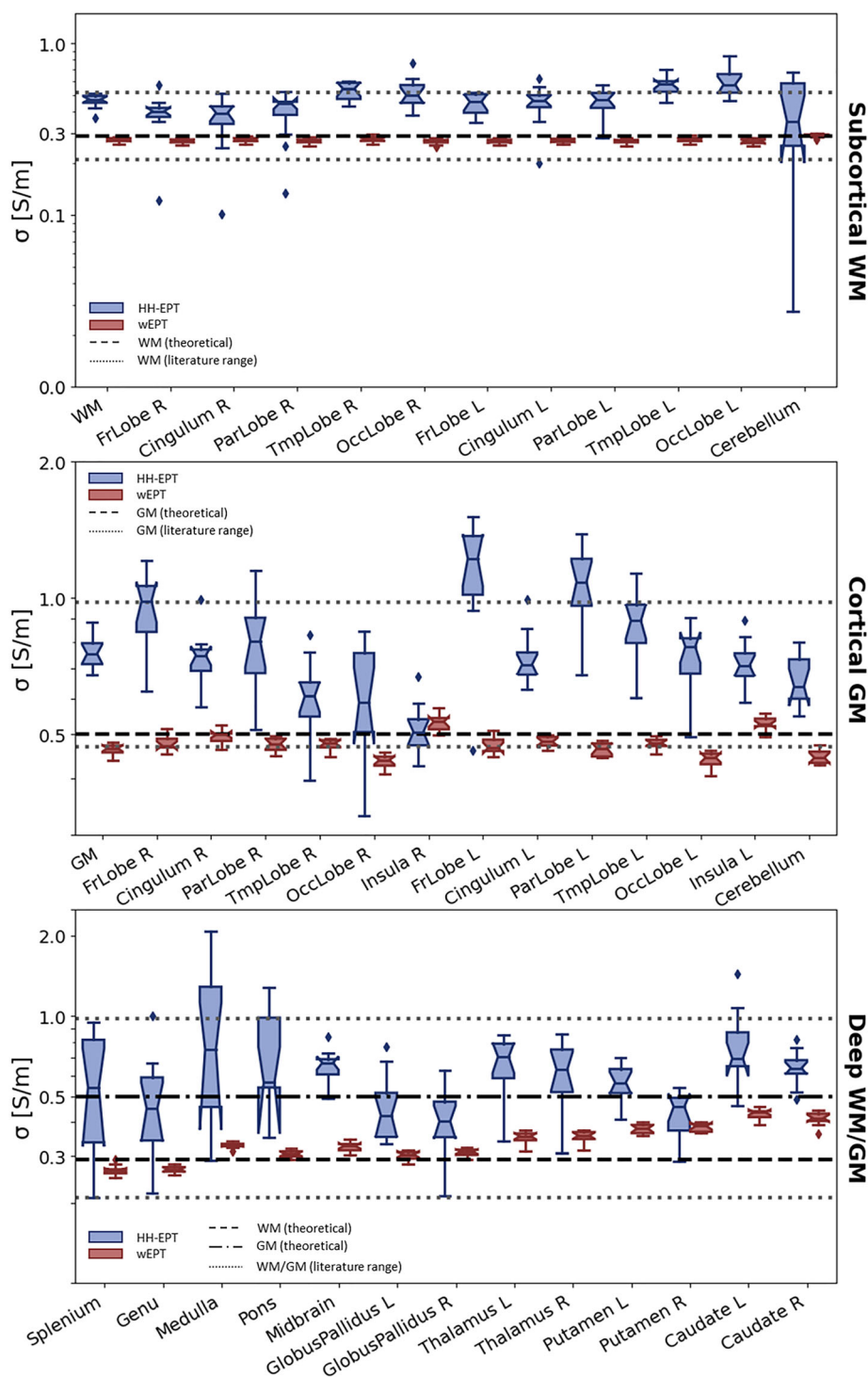


FIGURE 5 Box plots comparing bSSFP-based HH-EPT and QTI-based wEPT estimated conductivities for each ROI. Black lines mark the theoretical values for the WM and GM conductivities, while dotted lines mark the corresponding in vivo literature ranges. bSSFP, balanced steady-state free precession; GM, gray matter; HH-EPT, Helmholtz electrical properties tomography; QTI, Quantitative Transient-state Imaging; ROI, region of interest; wEPT, water content-based electrical properties tomography; WM, white matter.

values for WM and GM were consistently overestimated with respect to the reference values, both within the whole tissue masks and their different subregions. This can be explained by the assumption, used in this work, of uniform magnitude of the B_1^+ field in the conductivity reconstruction step. Even if this assumption is reasonable at 1.5 T, phase-only reconstruction may lead to such overestimation, as previously reported in the literature.⁴²

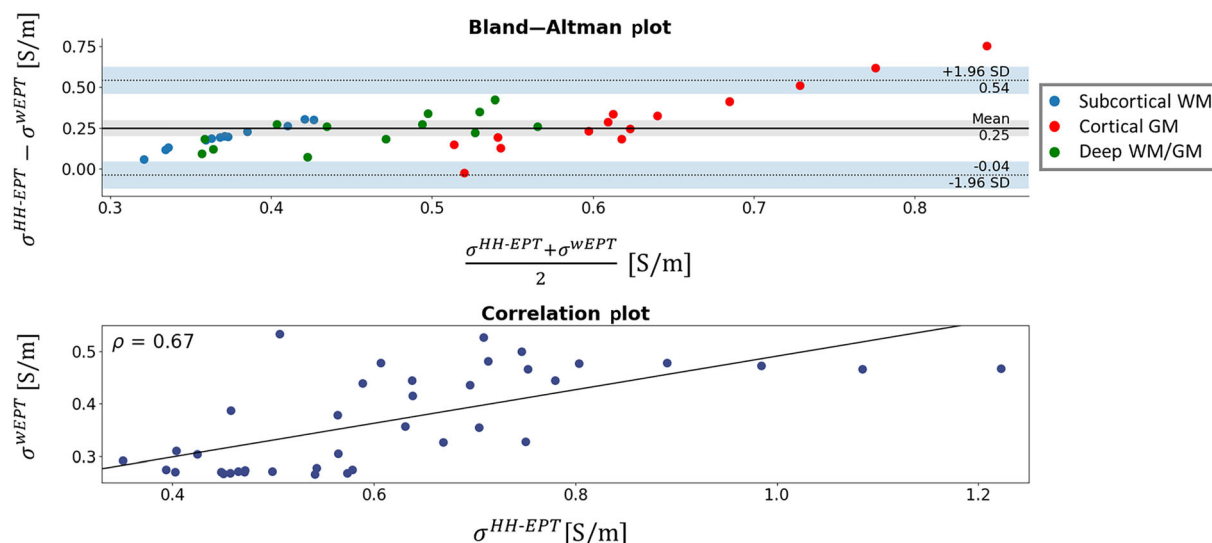


FIGURE 6 Comparison between bSSFP-based HH-EPT and QTI-based wEPT estimated conductivities. Top panel: Bland–Altman plot comparing the two methods. Blue, red, and green dots represent subcortical WM, cortical, and deep WM/GM ROIs, respectively. The solid black line and black dotted lines represent the mean and limit of agreement (here, $1.96 \times$ standard deviation). Gray and blue bands represent the 95% confidence intervals on mean and limit of agreement, respectively. Bottom panel: plot showing moderate correlation ($\rho = 0.67$, $p < 0.001$) between the conductivity values measured using the two approaches. bSSFP, balanced steady-state free precession; GM, gray matter; HH-EPT, Helmholtz electrical properties tomography; QTI, Quantitative Transient-state Imaging; ROI, region of interest; wEPT, water content-based electrical properties tomography; WM, white matter.

Overall, our results are in line with previous *in vivo* findings at the same field strength.³⁴ Despite the higher sensitivity to noise and system imperfection of HH-EPT, we found a moderate correlation between the two methods, suggesting that the ROIs heterogeneity revealed by wEPT reflects an actual spatial variability of the tissue properties. This is further supported by the comparison with the wEPT findings from Michel et al.,¹⁰ obtained by estimating electrical properties at 64 MHz from the water content values they reported. While a general quantification difference was found between QTI- and SE-based wEPT, probably because of the different magnetization transfer effect impacting the T_1 estimation,⁴³ the two methods showed a strong correlation for both conductivity and relative permittivity.

Compared with HH-EPT, the QTI-based wEPT technique demonstrated several advantages. First, data are processed voxel by voxel, preserving the resolution of the input data and avoiding blurring and loss of resolution caused by the local fitting windows used in HH-EPT. In addition, voxel-by-voxel processing avoids artifacts at different tissues interfaces: in HH-EPT, computation of conductivity from B_1^+ phase requires the inclusion of anatomical priors to reduce the tissue border effect, either via direct segmentation or coregistration of external tissue masks, potentially introducing additional errors. While advanced phase processing methods³¹ could further mitigate this artifact, as shown in Figure S2, voxel-by-voxel fitting of wEPT remains superior in this aspect.

Second, processing of T_1 maps only involves the evaluation of two simple analytical functions, which can be easily parallelized without any specialized hardware, thus reducing the inference time.

Third, wEPT also provides relative permittivity maps of the tissue, even at low field strengths such as 1.5 T, which are challenging to obtain using transmit field-based methods.⁴² Finally, as water content is frequency independent, the proposed technique could be used to calculate subject-specific electric properties maps at different frequencies, provided that the frequency is high enough for the underlying wEPT assumptions to be valid,^{44,45} that is, between 10 MHz and 1 GHz. These could be used in different medical applications beyond diagnosis itself, such as planning for microwave hyperthermia cancer treatment⁴⁶ and SAR prediction for RF pulse design.^{47–49}

These benefits are shared with the original wEPT implementation¹⁰ introduced by Michel et al. Changing the underlying sequence used to perform the water content mapping from a conventional T_1 -weighted SE acquisition to a quantitative transient-state method brings significant additional advantages. First, the direct use of a T_1 map, instead of the ratio R of two T_1 -weighted images for water content estimation, reduces the potential source of quantification biases. In fact, water content quantification from tissue T_1 is based solely on an empirical model, derived from histopathological observation, linking these two quantities. On the other hand, the estimation of water content from R is also based on other assumptions, namely, constant signal gain between the two different SE images and an additional empirical relation linking R and the water content, each potentially introducing other biases. Second, wEPT estimations based on SE acquisition have been shown to be affected by B_1^+ inhomogeneities,¹⁵ especially at high field strengths. Compensation of this quantification bias requires the acquisition of external B_1^+ maps, which increase the acquisition time, potentially leading to noise amplification, and might be affected by alignment errors. On the other hand, transient

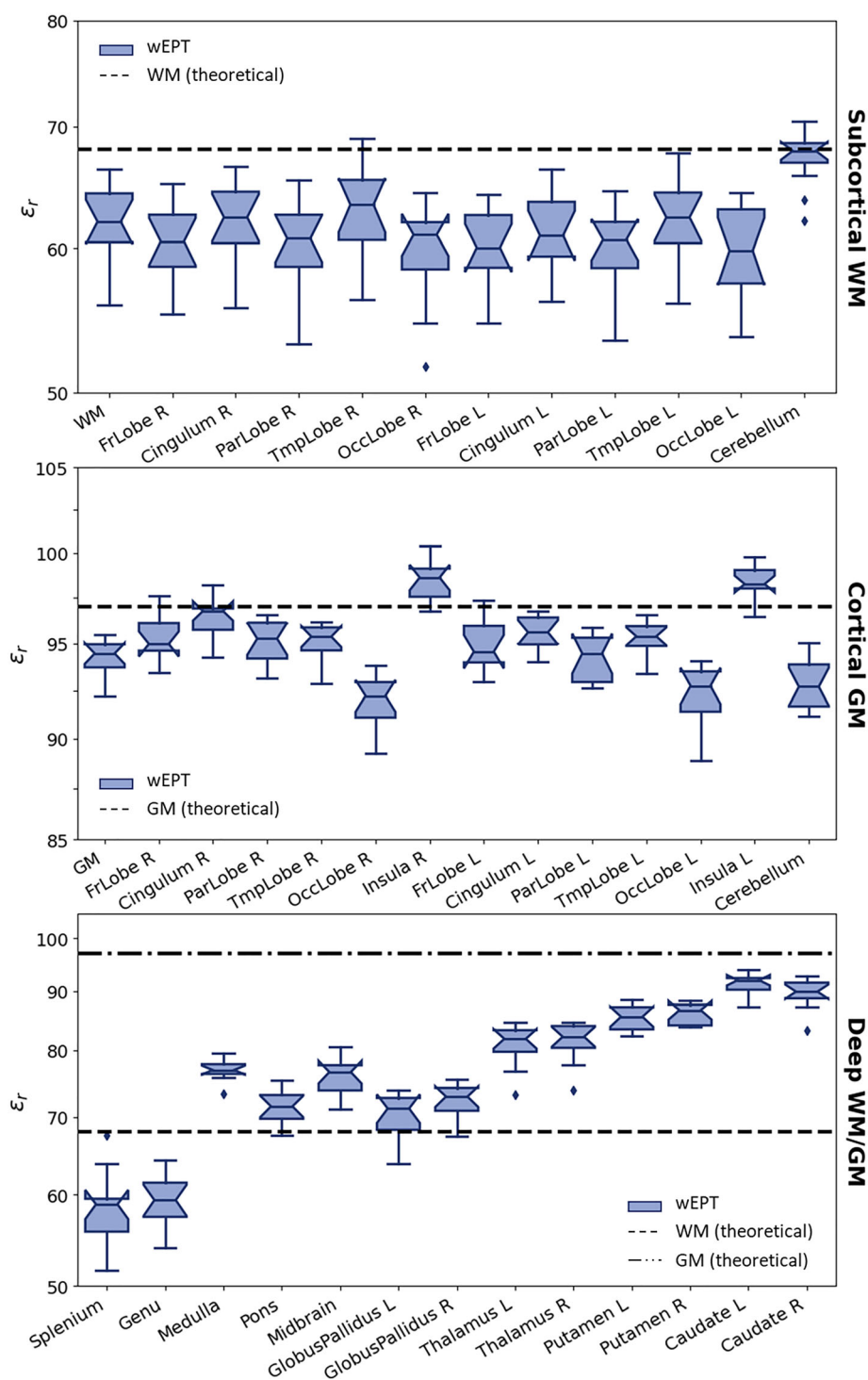


FIGURE 7 Box plots showing QTI-based wEPT estimated relative permittivity for each ROI. Black lines mark the theoretical values for the WM and GM relative permittivities. GM, gray matter; QTI, Quantitative Transient-state Imaging; ROI, region of interest; wEPT, water content-based electrical properties tomography; WM, white matter.

state-based parameter mapping techniques such as MR fingerprinting or QTI have been demonstrated to provide robust T_1 quantification in the presence of B_1^+ field inhomogeneities at different field strengths.^{24,50} Third, as the underlying QTI method has demonstrated high quantification repeatability and reproducibility, especially for T_1 , it is reasonable to expect similar behavior for the conductivity and relative permittivity estimations. This would be particularly important for longitudinal assessment of pathologies. Finally, compared with a dual SE acquisition, QTI also provides M_0 , T_1 , and T_2 maps of the tissues, which can be used either for quantitative tissue assessment or to produce synthetic contrast-weighted images for visual inspection. Importantly, the overall QTI-based wEPT scan time remains comparable with the original wEPT

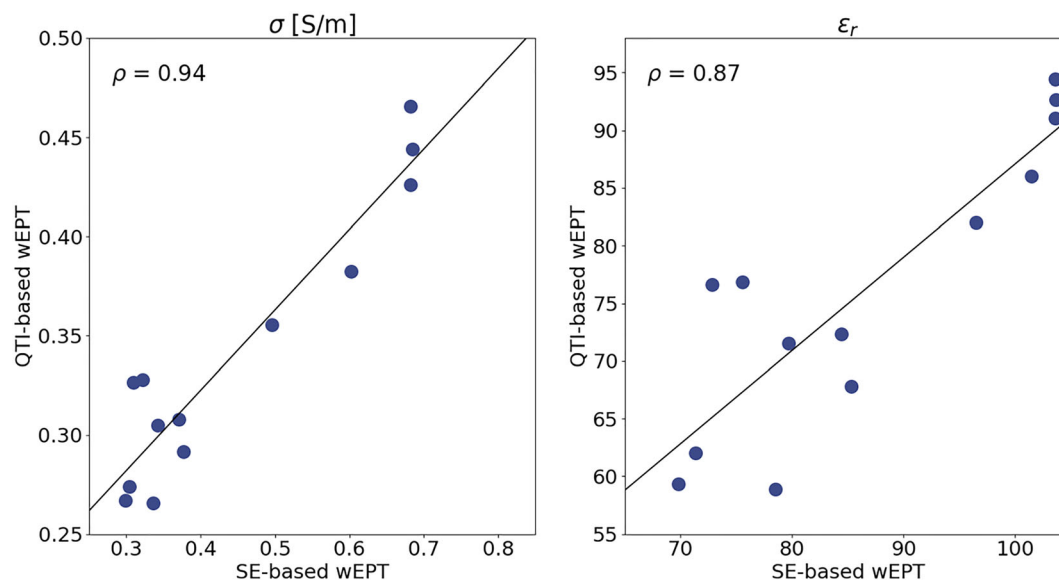


FIGURE 8 Comparison between the original SE-based wEPT implementation from Michel et al.¹⁰ and our QTI-based wEPT implementation. To enable the comparison, we used the water content values reported in Table 1 from Michel et al. to estimate conductivity and relative permittivity values for 1.5 T field strength. We restricted the comparison to the deep WM/GM ROIs, that is, those included in Michel et al.,¹⁰ grouping the left and right hemispheres. Both QTI-based wEPT conductivity and relative permittivity estimations show a strong Pearson's correlation (0.94/0.87, respectively, with $p < 0.001$) with the reference values from the Michel et al. publication. Correlation values ρ are displayed in each panel. GM, gray matter; QTI, Quantitative Transient-state Imaging; ROI, region of interest; wEPT, water content-based electrical properties tomography; WM, white matter.

approach, allowing its application in a clinical setting: the acquisition time for a QTI acquisition is 7 min, while the acquisition time for two SE sequences with the same spatial coverage and resolution with $TE = 11$ ms and $TR = 700$ ms/3000 ms, as described by Michel et al.,¹⁰ would be approximately 35 min (assuming a parallel imaging acceleration factor = 2).

While these advantages come at the cost of increased complexity in acquisition implementation and reconstruction, the recent development of open-source frameworks for pulse sequence design⁵¹ and reconstruction^{52,53} may alleviate this issue. The main limitation of the wEPT methods, including the proposed QTI-based technique, is that they do not rely on direct measurement of a physical quantity linked to the electrical properties by a physical model (as in transmit field-based techniques), but instead use a surrogate (i.e., the water content) based on an empirically observed correlation.⁵⁴ In order to completely assess the accuracy of QTI-based estimation, a ground truth measurement of conductivity and relative permittivity of the tissues would be required. However, our results are consistent with both theoretical predictions based on ex vivo measurements and previous literature findings obtained with transmit field-based methods^{34,55} in a relatively large cohort of healthy subjects ($n = 12$). Another limitation consists of the fact that the empirical model used to estimate the electrical properties from the water content is calibrated assuming that the same equations and coefficients hold for all the tissues. As demonstrated by,¹⁰ this is a reasonable assumption for high water content regions such as healthy brain tissues; generalization of the approach would require the inclusion of more tissue classes in the calibration, either from other histopathological studies or from other MR-based measurements,¹⁴ and is beyond the scope of the present work. Finally, the validation of this technique in pathological tissues remains an open challenge.^{56,57} While previous studies found correlation between water content and electrical properties even for pathological tissues (e.g., tumors),⁴⁴ this relationship might not hold for every possible condition. However, the nonlinear transformation used to obtain the electrical properties from T_1 may highlight subtle variation of the T_1 of the tissues, representing an alternative contrast to conventional T_1 - and T_2 -weighting in visual inspection. Our preliminary retrospective analysis of MS patient wEPT data provided promising results in this direction, showing potentially clearer lesion delineation compared with conventional contrast-weighted imaging. While not conclusive, the experiment showed the potential of electric properties as a quantitative biomarker, demonstrating a significant increase in both electrical conductivity and relative permittivity of pathological tissues with respect to normal-appearing WM, consistent with previous phase-based EPT results.⁵⁸ Future work will be focused on the quantitative assessment of QTI-based wEPT repeatability and reproducibility and its validation in pathologies using independent MR-EPT measurements and a larger cohort of patients, as well as extending this approach to other anatomical regions and optimizing the calibration model.

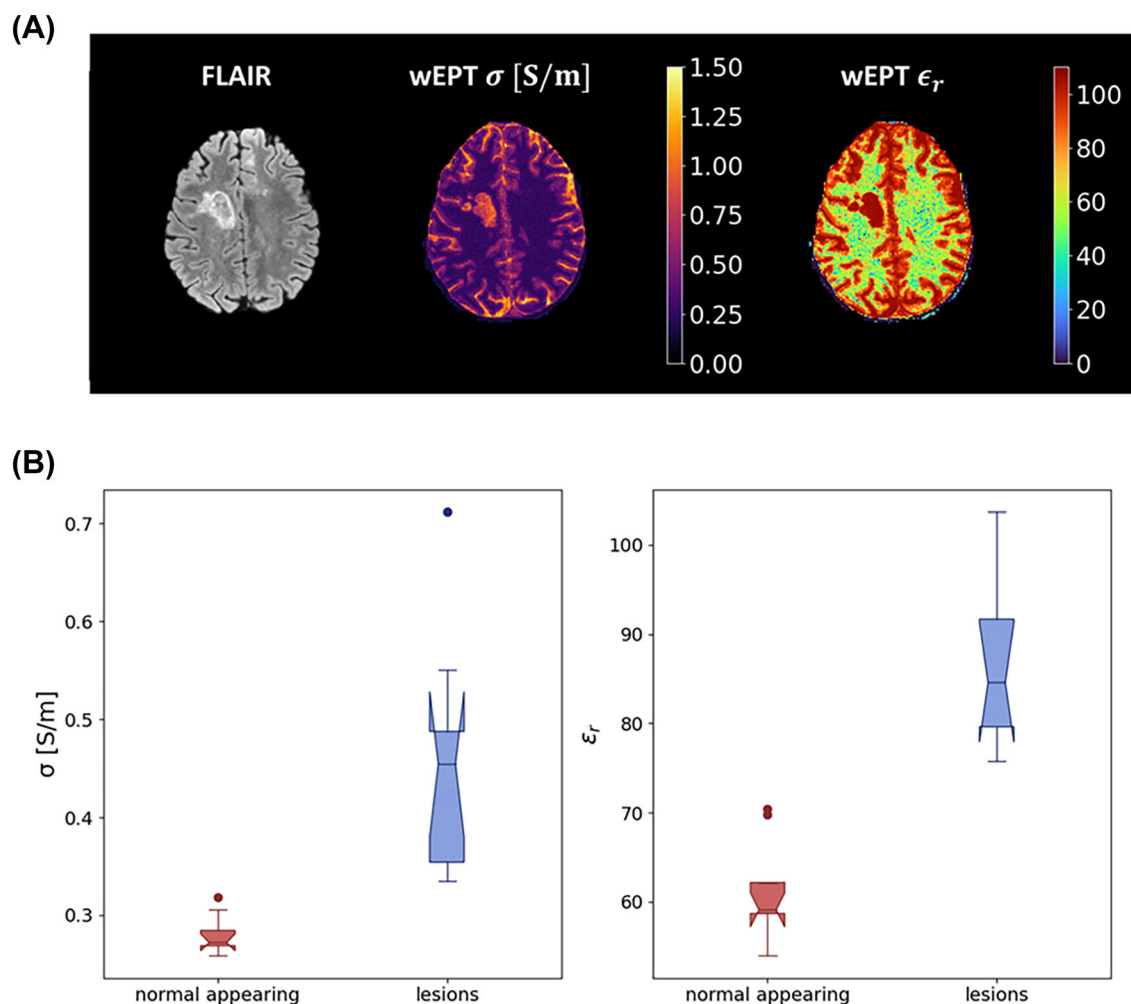


FIGURE 9 (A) Example of QTI-based wEPT application on a MS patient. It can be seen that the MS lesion appears to have higher conductivity (σ) and relative permittivity (ϵ_r) values compared with the surrounding WM in the wEPT acquisition. Moreover, QTI-based wEPT is able to resolve three separated structures that appear as a single lesion in a conventional FLAIR image of similar resolution. (B) Box plot representing electrical conductivity values (left) and relative permittivity (right) for normal-appearing WM and lesions. Abnormal tissues exhibit significantly higher values compared with normal-appearing WM ($p < 0.001$). FLAIR, FLuid Attenuated Inversion Recovery; MS, multiple sclerosis; QTI, Quantitative Transient-state Imaging; wEPT, water content-based electrical properties tomography; WM, white matter.

5 | CONCLUSIONS

We demonstrated that QTI is able to robustly map electrical properties of healthy brain tissue in addition to T_1 , T_2 , and M_0 within a short scan time, potentially paving the way for the application of EPT to clinical research. Importantly, while phase-only HH-EPT only provides conductivity values, QTI-based wEPT also enables relative permittivity estimation.

ACKNOWLEDGMENTS

The results presented here have been developed in the framework of the 18HLT05 QUIERO Project. This project has received funding from the EMPIR Programme co-financed by the Participating States and from the European Union's Horizon 2020 Research and Innovation Programme (18HLT05QUIERO). This work has been partially supported also by the Italian Ministry of Health under the grant RCLinea4 to IRCCS Fondazione Stella Maris. Open access funding provided by BIBLIOSAN.

CONFLICT OF INTEREST STATEMENT

This study was partially supported by a research grant from GE HealthCare. Rolf Schulte and Carolin Pirkl are GE HealthCare employees. All the other authors declare no other conflict of interest.

ORCID

Marta Lancione  <https://orcid.org/0000-0001-8911-7878>

REFERENCES

1. Surowiec AJ, Stuchly SS, Barr JR, Swarup A. Dielectric properties of breast carcinoma and the surrounding tissues. *IEEE Trans Biomed Eng.* 1988;35(4): 257-263. doi:[10.1109/10.1374](https://doi.org/10.1109/10.1374)
2. Haemmerich D, Staelin ST, Tsai JZ, Tungjitkusolmun S, Mahvi DM, Webster JG. In vivo electrical conductivity of hepatic tumours. *Physiol Meas.* 2003; 24(2):251-260. doi:[10.1088/0967-3334/24/2/302](https://doi.org/10.1088/0967-3334/24/2/302)
3. Schaefer M, Gross W, Ackemann J, Gebhard MM. The complex dielectric spectrum of heart tissue during ischemia. *Bioelectrochemistry Amst Neth.* 2002;58(2):171-180. doi:[10.1016/s1567-5394\(02\)00152-4](https://doi.org/10.1016/s1567-5394(02)00152-4)
4. Liu L, Dong W, Ji X, et al. A new method of noninvasive brain-edema monitoring in stroke: cerebral electrical impedance measurement. *Neurol Res.* 2006;28(1):31-37. doi:[10.1179/016164106X91843](https://doi.org/10.1179/016164106X91843)
5. Collins CM, Liu W, Wang J, et al. Temperature and SAR calculations for a human head within volume and surface coils at 64 and 300 MHz. *J Magn Reson Imaging.* 2004;19(5):650-656. doi:[10.1002/jmri.20041](https://doi.org/10.1002/jmri.20041)
6. Haacke EM, Petropoulos LS, Nilges EW, Wu DH. Extraction of conductivity and permittivity using magnetic resonance imaging. *Phys Med Biol.* 1991; 36(6):723-734. doi:[10.1088/0031-9155/36/6/002](https://doi.org/10.1088/0031-9155/36/6/002)
7. Katscher U, Kim DH, Seo JK. Recent progress and future challenges in MR electric properties tomography. *Comput Math Methods Med.* 2013;2013: 546562. doi:[10.1155/2013/546562](https://doi.org/10.1155/2013/546562)
8. Leijssen R, Brink W, van den Berg C, Webb A, Remis R. Electrical properties tomography: a methodological review. *Diagnostics.* 2021;11(2):176. doi:[10.3390/diagnostics11020176](https://doi.org/10.3390/diagnostics11020176)
9. Arduino A. EPTlib: an open-source extensible collection of electric properties tomography techniques. *Appl Sci.* 2021;11(7):3237. doi:[10.3390/app11073237](https://doi.org/10.3390/app11073237)
10. Michel E, Hernandez D, Lee SY. Electrical conductivity and permittivity maps of brain tissues derived from water content based on T1-weighted acquisition. *Magn Reson Med.* 2017;77(3):1094-1103. doi:[10.1002/mrm.26193](https://doi.org/10.1002/mrm.26193)
11. Fatouros PP, Marmarou A. Use of magnetic resonance imaging for in vivo measurements of water content in human brain: method and normal values. *J Neurosurg.* 1999;90(1):109-115. doi:[10.3171/jns.1999.90.1.0109](https://doi.org/10.3171/jns.1999.90.1.0109)
12. Wenger C, Hershkovich HS, Tempel-Brami C, Giladi M, Bomzon Z. Water-content electrical property tomography (wEPT) for mapping brain tissue conductivity in the 200–1000 kHz range: results of an animal study. In: Makarov S, Horner M, Noetscher G, eds. *Brain and human body modeling: computational human modeling at EMBC 2018*. Springer; 2019. doi:[10.1007/978-3-030-21293-3_20](https://doi.org/10.1007/978-3-030-21293-3_20)
13. Marino M, Cordero-Grande L, Mantini D, Ferrazzi G. Conductivity tensor imaging of the human brain using water mapping techniques. *Front Neurosci.* 2021;15:694645. doi:[10.3389/fnins.2021.694645](https://doi.org/10.3389/fnins.2021.694645)
14. Mandija S, Petrov PI, Vink JJT, Neggers SFW, Luijten PR, van den Berg CAT. In-vivo validation of water content electrical properties tomography reconstructions in white matter using independent MR-EPT measurements. In: *Proc 26th Sci Meet Int Soc Mag Reson Med Paris (FR)*. 2018:5096.
15. Han J, Gao Y, Nan X, Yu X, Liu F, Xin SX. Effect of radiofrequency inhomogeneity on water-content based electrical properties tomography and its correction by flip angle maps. *Magn Reson Imaging.* 2021;78:25-34. doi:[10.1016/j.mri.2020.12.020](https://doi.org/10.1016/j.mri.2020.12.020)
16. Ma D, Gulani V, Seiberlich N, et al. Magnetic resonance fingerprinting. *Nature.* 2013;495(7440):187-192. doi:[10.1038/nature11971](https://doi.org/10.1038/nature11971)
17. Sbrizzi A, van der Heide O, Cloos M, et al. Fast quantitative MRI as a nonlinear tomography problem. *Magn Reson Imaging.* 2018;46:56-63. doi:[10.1016/j.mri.2017.10.015](https://doi.org/10.1016/j.mri.2017.10.015)
18. Gómez PA, Molina-Romero M, Buonincontri G, Menzel MI, Menze BH. Designing contrasts for rapid, simultaneous parameter quantification and flow visualization with quantitative transient-state imaging. *Sci Rep.* 2019;9(1):8468. doi:[10.1038/s41598-019-44832-w](https://doi.org/10.1038/s41598-019-44832-w)
19. Jiang Y, Ma D, Keenan KE, Stupic KF, Gulani V, Griswold MA. Repeatability of magnetic resonance fingerprinting T1 and T2 estimates assessed using the ISMRM/NIST MRI system phantom. *Magn Reson Med.* 2017;78(4):1452-1457. doi:[10.1002/mrm.26509](https://doi.org/10.1002/mrm.26509)
20. Kördörfer G, Kirsch R, Liu K, et al. Reproducibility and repeatability of MR fingerprinting relaxometry in the human brain. *Radiology.* 2019;292(2): 429-437. doi:[10.1148/radiol.2019182360](https://doi.org/10.1148/radiol.2019182360)
21. Konar AS, Qian E, Geethanath S, et al. Quantitative imaging metrics derived from magnetic resonance fingerprinting using ISMRM/NIST MRI system phantom: an international multi-center repeatability and reproducibility study. *Med Phys.* 2021;48(5):2438-2447. doi:[10.1002/mp.14833](https://doi.org/10.1002/mp.14833)
22. Buonincontri G, Biagi L, Retico A, et al. Multi-site repeatability and reproducibility of MR fingerprinting of the healthy brain at 1.5 and 3.0 T. *Neuroimage.* 2019;195:362-372. doi:[10.1016/j.neuroimage.2019.03.047](https://doi.org/10.1016/j.neuroimage.2019.03.047)
23. Buonincontri G, Kurzwski JW, Kaggie JD, et al. Three dimensional MRF obtains highly repeatable and reproducible multi-parametric estimations in the healthy human brain at 1.5T and 3T. *Neuroimage.* 2021;226:117573. doi:[10.1016/j.neuroimage.2020.117573](https://doi.org/10.1016/j.neuroimage.2020.117573)
24. Buonincontri G, Sawiak SJ. MR fingerprinting with simultaneous B1 estimation. *Magn Reson Med.* 2016;76(4):1127-1135. doi:[10.1002/mrm.26009](https://doi.org/10.1002/mrm.26009)
25. Gómez PA, Cencini M, Golbabaee M, et al. Rapid three-dimensional multiparametric MRI with quantitative transient-state imaging. *Sci Rep.* 2020; 10(1):13769. doi:[10.1038/s41598-020-70789-2](https://doi.org/10.1038/s41598-020-70789-2)
26. Kurzwski JW, Cencini M, Peretti L, et al. Retrospective rigid motion correction of three-dimensional magnetic resonance fingerprinting of the human brain. *Magn Reson Med.* 2020;84(5):2606-2615. doi:[10.1002/mrm.28301](https://doi.org/10.1002/mrm.28301)
27. Jiang Y, Ma D, Seiberlich N, Gulani V, Griswold MA. MR fingerprinting using fast imaging with steady state precession (FISP) with spiral readout. *Magn Reson Med.* 2015;74(6):1621-1631. doi:[10.1002/mrm.25559](https://doi.org/10.1002/mrm.25559)
28. McGivney DF, Pierre E, Ma D, et al. SVD compression for magnetic resonance fingerprinting in the time domain. *IEEE Trans Med Imaging.* 2014;33(12): 2311-2322. doi:[10.1109/TMI.2014.2337321](https://doi.org/10.1109/TMI.2014.2337321)
29. Shah NJ, Abbas Z, Ridder D, Zimmermann M, Oros-Peusquens AM. A novel MRI-based quantitative water content atlas of the human brain. *Neuroimage.* 2022;252:119014. doi:[10.1016/j.neuroimage.2022.119014](https://doi.org/10.1016/j.neuroimage.2022.119014)
30. De Geeter N, Crevecoeur G, Dupré L, Van Hecke W, Leemans A. A DTI-based model for TMS using the independent impedance method with frequency-dependent tissue parameters. *Phys Med Biol.* 2012;57(8):2169-2188. doi:[10.1088/0031-9155/57/8/2169](https://doi.org/10.1088/0031-9155/57/8/2169)

31. Karsa A, Shmueli K. New approaches for simultaneous noise suppression and edge preservation to achieve accurate quantitative conductivity mapping in noisy images. In: *Proc Sci Meet Int Soc Mag Reson Med*. 2021:3774.
32. Friston KJ, Holmes AP, Worsley KJ, Poline JP, Frith CD, Frackowiak RSJ. Statistical parametric maps in functional imaging: a general linear approach. *Hum Brain Mapp*. 1994;2(4):189-210. doi:10.1002/hbm.460020402
33. Jenkinson M, Beckmann CF, Behrens TEJ, Woolrich MW, Smith SM. FSL. *Neuroimage*. 2012;62(2):782-790. doi:10.1016/j.neuroimage.2011.09.015
34. Voigt T, Katscher U, Doessel O. Quantitative conductivity and permittivity imaging of the human brain using electric properties tomography. *Magn Reson Med*. 2011;66(2):456-466. doi:10.1002/mrm.22832
35. Lee J, Shin J, Kim DH. MR-based conductivity imaging using multiple receiver coils. *Magn Reson Med*. 2016;76(2):530-539. doi:10.1002/mrm.25891
36. Avants BB, Epstein CL, Grossman M, Gee JC. Symmetric diffeomorphic image registration with cross-correlation: evaluating automated labeling of elderly and neurodegenerative brain. *Med Image Anal*. 2008;12(1):26-41. doi:10.1016/j.media.2007.06.004
37. Damasio H. *Human brain anatomy in computerized images*. Vol. xv. 2nd ed. Oxford University Press; 2005:540. doi:10.1093/acprof:oso/9780195165616.001.0001
38. Joshi AA, Shattuck DW, Leahy RM. A method for automated cortical surface registration and labeling. In: Dawant BM, Christensen GE, Fitzpatrick JM, Rueckert D, eds. *Biomedical image registration*. Lecture notes in computer science. Springer; 2012:180-189. doi:10.1007/978-3-642-31340-0_19
39. Dvorak AV, Swift-LaPointe T, Vavasour IM, et al. An atlas for human brain myelin content throughout the adult life span. *Sci Rep*. 2021;11(1):269. doi:10.1038/s41598-020-79540-3
40. Hasan KM, Walimuni IS, Kramer LA, Narayana PA. Human brain iron mapping using atlas-based T2 relaxometry. *Magn Reson Med*. 2012;67(3):731-739. doi:10.1002/mrm.23054
41. Ridley B, Morsillo F, Zaaroui W, Nonino F. Variability by region and method in human brain sodium concentrations estimated by ²³Na magnetic resonance imaging: a meta-analysis. *Sci Rep*. 2023;13(1):3222. doi:10.1038/s41598-023-30363-y
42. van Lier ALHMW, Raaijmakers A, Voigt T, et al. Electrical properties tomography in the human brain at 1.5, 3, and 7T: a comparison study. *Magn Reson Med*. 2014;71(1):354-363. doi:10.1002/mrm.24637
43. Teixeira AGRP, Malik SJ, Hajnal JV. Fast quantitative MRI using controlled saturation magnetization transfer. *Magn Reson Med*. 2019;81(2):907-920. doi:10.1002/mrm.27442
44. Schepps JL, Foster KR. The UHF and microwave dielectric properties of normal and tumour tissues: variation in dielectric properties with tissue water content. *Phys Med Biol*. 1980;25(6):1149-1159. doi:10.1088/0031-9155/25/6/012
45. Farace P, Pontalti R, Cristoforetti L, Antolini R, Scarpa M. An automated method for mapping human tissue permittivities by MRI in hyperthermia treatment planning. *Phys Med Biol*. 1997;42(11):2159-2174. doi:10.1088/0031-9155/42/11/011
46. Tsuda N, Kuroda K, Suzuki Y. An inverse method to optimize heating conditions in RF-capacitive hyperthermia. *IEEE Trans Biomed Eng*. 1996;43(10):1029-1037. doi:10.1109/10.536904
47. Voigt T, Homann H, Katscher U, Doessel O. Patient-individual local SAR determination: in vivo measurements and numerical validation. *Magn Reson Med*. 2012;68(4):1117-1126. doi:10.1002/mrm.23322
48. Buchenau S, Haas M, Splitthoff DN, Hennig J, Zaitsev M. Iterative separation of transmit and receive phase contributions and B1(+)-based estimation of the specific absorption rate for transmit arrays. *MAGMA*. 2013;26(5):463-476. doi:10.1007/s10334-013-0367-6
49. Zhang X, Van de Moortele PF, Liu J, Schmitter S, He B. Quantitative prediction of radio frequency induced local heating derived from measured magnetic field maps in magnetic resonance imaging: a phantom validation at 7 T. *Appl Phys Lett*. 2014;105(24):244101. doi:10.1063/1.4903774
50. Buonincontri G, Schulte RF, Cosottini M, Tosetti M. Spiral MR fingerprinting at 7T with simultaneous B1 estimation. *Magn Reson Imaging*. 2017;41:1-6. doi:10.1016/j.mri.2017.04.003
51. Layton KJ, Kroboth S, Jia F, et al. Pulseseq: a rapid and hardware-independent pulse sequence prototyping framework. *Magn Reson Med*. 2017;77(4):1544-1552. doi:10.1002/mrm.26235
52. Hansen MS, Sørensen TS. Gadgetron: an open source framework for medical image reconstruction. *Magn Reson Med*. 2013;69(6):1768-1776. doi:10.1002/mrm.24389
53. Knopp T, Grosser M. MRIReco.jl: an MRI reconstruction framework written in Julia. *Magn Reson Med*. 2021;86(3):1633-1646. doi:10.1002/mrm.28792
54. Mandija S, de Bruin PW, Webb AG, Luijten PR, van den Berg CAT. Investigating the relation between electrical conduction and tissue composition with proton and sodium MRI. In: *Proc 25th Sci Meet Int Soc Mag Reson Med Honolulu, Hawaii (US)*. 2017:3639.
55. Mandija S, Petrov PI, Vink JJT, Neggers SFW, van den Berg CAT. Brain tissue conductivity measurements with MR-electrical properties tomography: an in vivo study. *Brain Topogr*. 2021;34(1):56-63. doi:10.1007/s10548-020-00813-1
56. Liao Y, Oros-Peusquens AM, Lindemeyer J, et al. An MR technique for simultaneous quantitative imaging of water content, conductivity and susceptibility, with application to brain tumours using a 3T hybrid MR-PET scanner. *Sci Rep*. 2019;9(1):88. doi:10.1038/s41598-018-36435-8
57. Katscher U, Tha KK. Normalization of conductivity maps to support identification of pathologic areas. In: *Proc 31st Sci Meet Int Soc Mag Reson Med London (UK)*. 2022:3296.
58. Huhndorf M, Stehning C, Rohr A, et al. EPT—measurement of brain conductivity for non-oncologic applications. In: *Proc 23rd Sci Meet Int Soc Mag Reson Med Toronto (CAN)*. 2015:2194.

SUPPORTING INFORMATION

Additional supporting information can be found online in the Supporting Information section at the end of this article.

How to cite this article: Cencini M, Lancione M, Pasquariello R, et al. Fast high-resolution electric properties tomography using three-dimensional quantitative transient-state imaging-based water fraction estimation. *NMR in Biomedicine*. 2023;e5039. doi:10.1002/nbm.5039